REPORT DOCUMENTATION PAGE

Form Approved
OMB No. 0704-0188

The public reporting burden for this collection of information is estimated to average 1 hour per response, including the time for reviewing instructions, searching existing data sources, gathering and maintaining the data needed, and completing and reviewing the collection of information. Send comments regarding this burden estimate or any other aspect of this collection of information, including suggestions for reducing the burden, to the Department of Defense, Executive Service Directorate (0704-0188). Respondents should be aware that notwithstanding any other provision of law, no person shall be subject to any penalty for failing to comply with a collection of information if it does not display a currently valid OMB control number.

PLEASE DO NOT RETURN YOUR FORM TO THE ABOVE ORGANIZATION.

1. REPORT DATE *(DD-MM-YYYY)*	2. REPORT TYPE	3. DATES COVERED *(From - To)*
04-19-2017	Conference paper	1 Jan 2013 - 1 Aug 2014

4. TITLE AND SUBTITLE
Attitude Determination and Control System Design for a 6U CubeSat for Proximity Operations and Rendezvous

5a. CONTRACT NUMBER
N/A

5b. GRANT NUMBER
N/A

5c. PROGRAM ELEMENT NUMBER
N/A

6. AUTHOR(S)
Francisco J. Franquiz, Peter Edwards, Bogdan Udrea, Michael Nayak, Thorsten Pueschl

5d. PROJECT NUMBER
N/A

5e. TASK NUMBER
N/A

5f. WORK UNIT NUMBER
N/A

7. PERFORMING ORGANIZATION NAME(S) AND ADDRESS(ES)
Air Force Institute of Technology, 2950 Hobson Way, Wright Patterson AFB, OH 45433
Embry-Riddle Aeronautical University, 600 S Clyde Morris Blvd, Daytona Beach FL 32114
dSPACE GmbH, Paderborn, 32102, Germany

8. PERFORMING ORGANIZATION REPORT NUMBER
N/A

9. SPONSORING/MONITORING AGENCY NAME(S) AND ADDRESS(ES)
Air Force Institute of Technology, 2950 Hobson Way, Wright Patterson AFB, OH 45433

10. SPONSOR/MONITOR'S ACRONYM(S)
AFIT/CIP

11. SPONSOR/MONITOR'S REPORT NUMBER(S)
N/A

12. DISTRIBUTION/AVAILABILITY STATEMENT
Distribution A. Approved for public release: distribution unlimited.

13. SUPPLEMENTARY NOTES
2014 AIAA Space Conference and Exposition, 4-7 August 2014, San Diego, California, USA. ISBN: 9781634394604

14. ABSTRACT
The work presented in this paper focuses on the design of an attitude determination and control subsystem (ADCS) for a proximity operation and imaging satellite mission. The ARAPAIMA (Application for Resident Space Object Proximity Analysis and IMAging) mission is carried out by a 6U CubeSat class satellite equipped with a warm gas propulsion system. The propulsion system comprises an orbital maneuvering thruster which produces 100 mN and a set of 16 reaction control system (RCS) thrusters, of 25 mN each, installed in pairs that generate torques about each of the satellite body axes. The thrust of the RCS thrusters can be modulated over the entire range in steps of 1% due to the rapid solenoid valve actuation. The requirement of the control system is to provide pointing control accuracy of 1 arcmin at 3 deg in the desired imaging direction. The ADCS employs two control laws. One control law, for large angle maneuvers, implements eigenaxis maneuvering and the other, for accurate pointing, is implemented with PID controllers about each body axis. The integration of both controllers and accuracy are discussed.

15. SUBJECT TERMS
Nanosatellite, laser rangefinder, ARAPAIMA, USAF, object imaging, shape reconstruction, space-based, ISR, space situational awareness

16. SECURITY CLASSIFICATION OF:			17. LIMITATION OF ABSTRACT	18. NUMBER OF PAGES	19a. NAME OF RESPONSIBLE PERSON
a. REPORT	b. ABSTRACT	c. THIS PAGE			MICHAEL NAYAK
UU	UU	UU	NONE	12	19b. TELEPHONE NUMBER *(Include area code)* 808-891-7727

Reset

Standard Form 298 (Rev. 8/98)
Prescribed by ANSI Std. Z39.18
Adobe Professional 7.0

Attitude Determination and Control System Design for a 6U CubeSat for Proximity Operations and Rendezvous

Francisco J. Franquiz * , Peter Edwards † and Bogdan Udrea ‡
Embry-Riddle Aeronautical University, Daytona Beach, FL, 32114, USA

Michael V. Nayak §
Red Sky Research, Albuquerque, New Mexico, 87108, USA

Thorsten Pueschl ¶
dSPACE GmbH, Paderborn, 32102, Germany

The work presented in this paper focuses on the design of an attitude determination and control subsystem (ADCS) for a proximity operation and imaging satellite mission. The ARAPAIMA (Application for Resident Space Object Proximity Analysis and IMAging) mission is carried out by a 6 U CubeSat class satellite equipped with a warm gas propulsion system. The propulsion system comprises an orbital maneuvering thruster which produces 100 mN and a set of 16 reaction control system (RCS) thrusters, of 25 mN each, installed in pairs that generate torques about each of the satellite body axes. The thrust of the RCS thrusters can be modulated over the entire range in steps of 1% due to the rapid solenoid valve actuation. The requirement of the control system is to provide pointing control accuracy of 1 arcmin at 3 σ in the desired imaging direction. The ADCS employs two control laws. One control law, for large angle maneuvers, implements eigenaxis maneuvering and the other, for accurate pointing, is implemented with PID controllers about each body axis.

Simulations performed for tracking the resident space object flying in a circular orbit of 500 km altitude from a relative orbit of 250 m are used to test the performance of the ADCS. A comparison between a "traditional" ADCS system with reaction wheels and RCS thrusters for their off-loading, and a system with only RCS thrusters has been performed. The accuracy of the pointing is comparable, the pointing performance as well as the propellant usage for both options are further discussed in the paper. The integration of both controllers within the ADCS and the switching are also discussed.

Nomenclature

C_m	Moment coefficient
I_{sp}	Propellant specific impulse
J_p	Solar panel moment of inertia matrix
J_{rw}	Flywheel moment of inertia
K_m	Reaction wheel motor torque constant
Kn	Knudsen number
M_{sl}	Propellant slosh disturbance moment
N	Atomic nitrogen

*MS Candidate, Department of Aerospace Engineering, franquif@my.erau.edu
†MS Graduate, Department of Aerospace Engineering, edwardp1@my.erau.edu
‡Associate Professor, Department of Aerospace Engineering, udreab@erau.edu
§Principal Research Scientist, nayak@redskyresearch.org
¶Senior Application Engineer, tpueschl@dspace.de

O	Atomic oxygen
R_m	Reaction wheel motor resistance
S	Maximum projected satellite surface area
S_s	Sunlit surface area
T	RCS thrust
α	Angle of attack
β	Sideslip angle
$\boldsymbol{B_E}$	Earth's magnetic field vector at satellite location
$\boldsymbol{F_b}$	Force vector acting on the body-frame
$\boldsymbol{F_d}$	Disturbance force vector acting on the body-frame
$\boldsymbol{F_{cmd}}$	Controller Force Command
$\boldsymbol{H_{rw}}$	Reaction wheel angular momentum
$\boldsymbol{J_{rw}}$	Reaction wheel moment of inertia matrix
$\boldsymbol{J}$	Moment of inertia matrix
$\boldsymbol{M_b}$	Moment vector acting on the body-frame
$\boldsymbol{M_d}$	Disturbance moment vector acting on the body-frame
$\boldsymbol{M_{aero}}$	Aerodynamic disturbance moment
$\boldsymbol{M_{cmd}}$	Controller moment command
$\boldsymbol{M_{gg}}$	Gravity gradient disturbance moment
$\boldsymbol{M_p}$	Solar panel flexible mode disturbance moment
$\boldsymbol{M_{rmm}}$	Magnetic disturbance moment
$\boldsymbol{M_{srp}}$	Solar radiation pressure disturbance moment
$\boldsymbol{T_{cmd}}$	Controller thrust command at time
$\boldsymbol{V_\infty}$	Freestream velocity vector
$\boldsymbol{\Omega_{rw}}$	Reaction wheel angular velocity vector
$\boldsymbol{\Phi}$	Solar intensity vector
$\bar{\boldsymbol{\omega}}$	Angular velocity imaginary quaternion
$\bar{\boldsymbol{q}}$	Unit quaternion/Euler-Rodrigues parameters
$\dot{\boldsymbol{V}}_{\boldsymbol{b}}$	Velocity vector of the body-frame
$\hat{\boldsymbol{e}}$	Euler-axis unit vector
$\hat{\boldsymbol{r}}$	Satellite position unit vector in the ECI frame
$\boldsymbol{\omega}$	Angular velocity vector of the body-frame
$\boldsymbol{\theta_p}$	Solar panel position vector
$\boldsymbol{m_{rmm}}$	Residual magnetic dipole or moment
$\boldsymbol{q_v}$	Vector quaternion component
$\boldsymbol{r}$	Satellite's position vector in the ECI frame
λ	Atmospheric particle mean free path
μ	Earth's gravitational parameter
ω_e	Earth's angular velocity vector
ω_{rw}	Reaction wheel angular speed
ϕ	Euler angle parameter
ρ	Mass density
θ_{sl}	Mechanical slosh model angular displacement
ξ	Reflectance value of the satellite
b	Solar panel joint damping coefficient
c	Speed of light in a vacuum
f_s	Average solar constant
f_{rcs}	RCS thruster operating frequency
g_e	Gravity at Earth's surface
h_{rw}	Reaction wheel nominal angular momentum
$h_{sl,n}$	Mechanical slosh model angular momentum
k	Solar panel joint spring constant
$k_{i,rw}$	Reaction wheel controller integral gain
$k_{p,rw}$	Reaction wheel controller proportional gain
l	Reference length (shortest satellite body dimension)

l_s	Solar radiation pressure moment arm
l_{rcs}	RCS thruster moment arm
m	Satellite rigid-body mass
$m_{b,rw}$	Propellant mass per reaction wheel off-load maneuvers
m_{prop}	Propellant mass
m_{sl}	Mechanical slosh model mass
n	Number density
q_0	Scalar quaternion component
s	Laplace transform complex parameter
$x_{sl,n}$	Mechanical slosh model linear displacement

I. Introduction

With the increasing interest on low budget space missions, academia has found a niche in the space industry. Going further than proposals and designs, many universities have flown satellites as parts of military and governmental initiatives across the world. These satellites, better known as CubeSats (minuaturized satellites measured in 1 liter volume units or 1 U) , can be developed using commercial off-the-shelf (COTS) products which considerably lower the overall cost of missions. Recently, CubeSat missions have grown more ambitious in nature helped along by the current trend on miniaturized high performance optics, power systems, and other electronics. These missions now blur the line which distinguishes professional projects from those previously regarded as overreaching.

While encouraging, this upsurge brings a set of issues to address. As popularity and feasibility continue to rise so does the number of satellites launched each year. Each of these contribute to the amount of debris in low Earth orbit (LEO) (altitudes ranging from 160 km to 2000 km). Although this specific issue has recently been the focus of some publicity no final solution currently exists.

A. Arapaima Mission Overview

As a precursory component to the reduction of orbital debris, the ARAPAIMA mission proposes a reconnaissance approach to perform visible, infrared (IR), and 3D imaging of Resident Space Objects (RSOs) without a priori knowledge of their shape or attitude. This process follows a set of autonomous approach and close proximity maneuvers carried out with sufficient accuracy to allow rendezvous and docking maneuvers with the RSO.

The mission is carried out by a 12 kg 6 U (36.6 x 23.9 x 27.97) cm CubeSat (with an imaging array consisting of an IR camera, a miniature laser rangefinder, and a visible light monochrome camera arranged such that their respective imaging directions are parallel to each other as shown in figure 1.

To perform orbital approach maneuvers, the satellite is equipped with a difluoroethane warm gas propulsion system operated via rapid solenoid valve actuation and miniaturized 2D nozzle sets attached to the satellite body. The system is comprised of 16 RCS thrusters setup in pairs, each one capable of producing up to 25 mN of thrust. The thrusters are arranged such that 4 nozzles are parallel to each other in the x and z directions on the body frame (figure 2). These 4 nozzle clusters make up the orbital maneuvering thrusters (OMTs) and provide a total 100 mN of thrust.

Reaction attitude control is performed by operating the thrusters in pairs; these are positioned such that a pure moment can be exerted about each body axis. The number of thrusters and their placement provide a full layer of redundancy as the RCS system is able to operate with 4 nozzle pairs (pairs A B C D or E F G H in figure 2).

The satellite's attitude determination and control system (ADCS) uses a combination of startracker (STR) and inertial measurement unit (IMU) sensor readings to achieve a pointing control accuracy of 1 arcmin at 3σ in the desired direction of the imaging array (figure 1). The startracker has a boresight accuracy of 6 arcsec and a 40 arcsec roll axis accuracy. The IMU includes angular rate gyro ($\pm 150^{\circ}/s$ range) and accelerometer (± 2 g range) triads together with tri-axial magnetometer sensors (± 1.9 gauss). As a secondary attitude determination system, the satellite will also carry photodiode sun sensors. These are used during operational modes in which the startracker is unable to provide an attitude solution such as detumbling maneuvers. An onboard GPS module is utilized to track the position of the satellite during orbital maneuvers and complement the communications array.

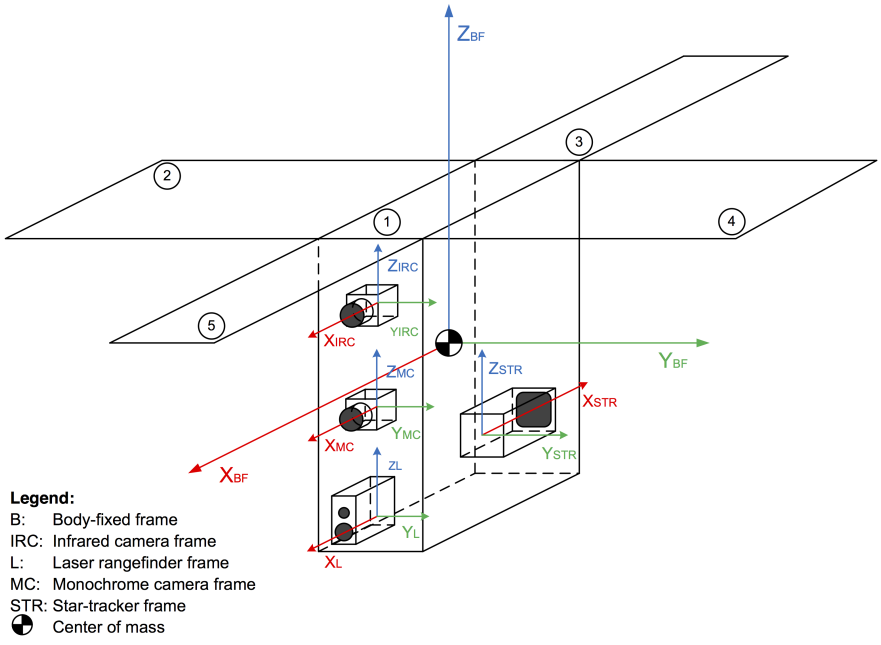

Figure 1: Imaging array placement on the satellite body. The x-axis on the satellite's body-fixed frame is defined as being parallel to the imaging direction.

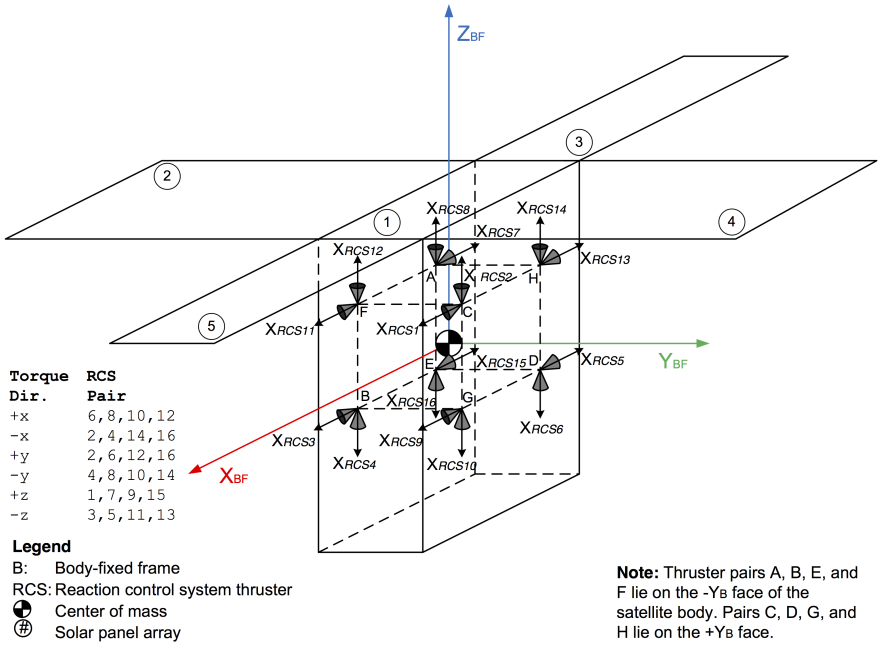

Figure 2: RCS thruster placement on satellite body-frame.

II. Dynamic Modeling

The satellite dynamics serving as the process or plant for the system were modeled as a combination of attitude kinematics and orbital mechanics for a rigid body with 6 degrees-of-freedom (DOF). These are further augmented by a set of environmental models and conditions which contribute to the external disturbances acting on the satellite body. Sources of internal disturbances are also considered.

A. Rigid-Body Dynamics

The satellite body is treated as a rigid body with constant mass and moment of inertia. The forces and moments acting on the satellite's body fixed frame are given by Eqs. (1) and (2) with the body-fixed frame defined as shown in figure 2.

$$\boldsymbol{F_b} = m(\dot{\boldsymbol{V}}_{\boldsymbol{b}} + \boldsymbol{\omega} \times \boldsymbol{V_b}) + \boldsymbol{F_d} + \boldsymbol{F_{cmd}} \tag{1}$$

$$\boldsymbol{M_b} = \boldsymbol{J}\dot{\boldsymbol{\omega}} \times (\boldsymbol{J\omega}) + \boldsymbol{M_d} + \boldsymbol{M_{cmd}} \tag{2}$$

Changes throughout the mission to the satellite's configuration such as when appendages (solar panels, antennas, etc.) are deployed are modeled as impulsive changes in its moment of inertia by corresponding moment disturbances . Additionally, for the purpose of attitude control simulations the mass flow rate of the propellant is assumed to be small enough for the mass to be considered constant throughout imaging maneuvers.

The attitude kinematics are described in terms of Euler-Rodrigues parameters or rotation quaternions. All quaternions referenced henceforth are considered to be normalized unit-quaternions and are defined as

$$\bar{\boldsymbol{q}} = \begin{bmatrix} q_0 \\ q_1 \\ q_2 \\ q_3 \end{bmatrix} = \begin{bmatrix} \cos(\phi/2) \\ \sin(\phi/2)\hat{e}_x \\ \sin(\phi/2)\hat{e}_y \\ \sin(\phi/2)\hat{e}_z \end{bmatrix} = \begin{bmatrix} \cos(\phi/2) \\ \sin(\phi/2)\hat{\boldsymbol{e}} \end{bmatrix} = \begin{bmatrix} q_0 \\ \boldsymbol{q_v} \end{bmatrix} \tag{3}$$

where $\hat{\boldsymbol{e}}$ is an arbitrary unit column vector and ϕ is an arbitrary angle through which a 3-dimensional frame is rotated about $\hat{\boldsymbol{e}}$ as given by Euler's formula[1]

$$R(\hat{\boldsymbol{e}}, \boldsymbol{\phi} = \cos(\phi)\boldsymbol{I} + (1 - \cos(\phi))\hat{\boldsymbol{e}}\hat{\boldsymbol{e}}^T + \cos\phi \tag{4}$$

The quaternion kinematic equation in terms of the inertial-referenced body angular velocity is then given by[1, 2]

$$\dot{\bar{\boldsymbol{q}}} = \frac{1}{2}\bar{\boldsymbol{q}} \otimes \bar{\boldsymbol{\omega}} \tag{5}$$

Or in matrix notation

$$\dot{\bar{\boldsymbol{q}}} = \frac{1}{2}\boldsymbol{\Omega(\omega)}\bar{\boldsymbol{q}} \tag{6}$$

where

$$\boldsymbol{\Omega(\omega)} = \begin{bmatrix} 0 & -\omega_x & -\omega_y & -\omega_z \\ \omega_x & 0 & \omega_z & -\omega_y \\ \omega_y & -\omega_z & 0 & \omega_x \\ \omega_z & \omega_y & -\omega_x & 0 \end{bmatrix} \tag{7}$$

Equations (1) and (2) along with Eq. (5) make up the full dynamics of the model and allow us to determine the satellite's state at any time t based on known initial conditions. All perturbations and inputs to the system are included directly into Eqs. (1) and (2) through the $\boldsymbol{F_d}$ and $\boldsymbol{M_d}$ terms respectively and are propagated through the integration of $\boldsymbol{\omega}$.

The error quaternion of the satellite is defined as the quaternion which describes the rotation from the current quaternion state to the desired or commanded quaternion. It is defined by quaternion algebra as

$$\bar{\boldsymbol{q}}_{\boldsymbol{e}} = \begin{pmatrix} q_{0,e} \\ \boldsymbol{q_{v,e}} \end{pmatrix} = \bar{\boldsymbol{q}}_{\boldsymbol{cmd}}^{-1} \otimes \bar{\boldsymbol{q}} \tag{8}$$

The pointing error is defined as the angle from the body x-axis (imaging direction) to the desired x-axis as given by the error quaternion. It can be easily calculated as

$$\psi_e = (q_{0,e}^2 + q_{1,e}^2 - q_{2,e}^2 - q_{3,e}^2) \tag{9}$$

B. Environmental Models

To account for environmental conditions and scenarios a set of models are set parallel with the dynamic equations discussed above. These shape the moments and forces acting on the system to mirror the scenario of a satellite in LEO at approximately 500 km from the Earth's surface. At this altitude, the effects of Earth's gravitational and magnetic field as well as its atmosphere are non-negligible. As such, they form the majority of the plant or process under consideration.

At this point in time it would also be useful to specify the reference frames utilized throughout the different models. The body frame has already been defined as seen in figures 1 and 2. The inertial frame is defined as the ECI (Earth-Centered Inertial) as described by the J2000 system[3] where the x-axis is aligned with the mean vernal equinox and the z-axis is aligned with the ω_e vector shown in figure 3. This frame is used for all internal calculations throughout the models and it serves as a reference point for transformations between different frames. Another useful frame is the ECEF (Earth-Centered Earth-Fixed) where the x-axis points to the (0°, 0°) point on the Earth's graticule and the z-axis is aligned with the ω_e vector. It should be noted, however, that because ECEF frame rotates with the Earth, the z-axis does not lie perfectly along ω_e due to polar motion.

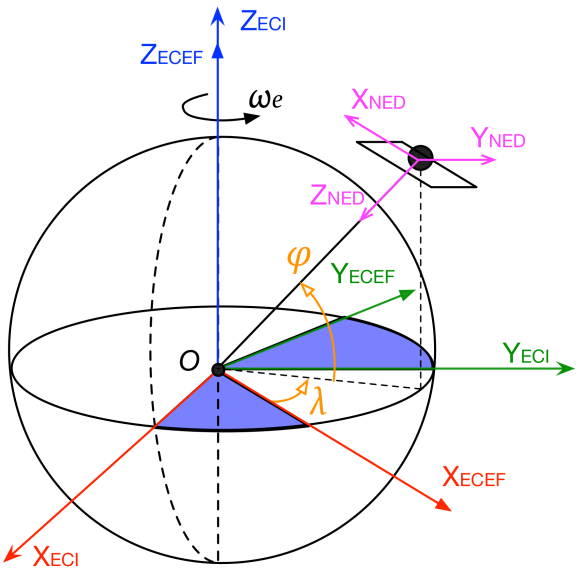

Figure 3: ECI, ECEF, and NED reference frames. The latitude (λ) and longitude (ϕ) convention for an arbitrary point over the Earth's surface with respect to the ECEF frame is shown.

Finally, some environmental models provide information on the North-East-Down (NED) frame, a type of noninertial, flat Earth (local tangent plane, LTP) reference system usually used for aircraft navigation.[4] In this system the x-axis points to the polar North (parallel to the LTP) while the z-axis points downward (nadir), towards the Earth's surface. The y-axis completes the right-handed frame and points East on the LTP (figure 3). Note that while the center of the NED frame is dependent on the body's location (relative to ECEF) the frame is not a body-fixed frame.

1. Gravitational Model

In order to have the body follow an orbital trajectory, a gravitational model is used to determine the force acting on the satellite at any point in time. The model implements the mathematical representation of the geocentric equipotential ellipsoid described by the 1984 World Geodetic System (WGS84).[2] The model is able to determine the Earth's gravity at any specific location on the ECI frame limited only by the geodetic height. By initializing latitude, longitude, and altitude parameters at the expected launch date, any desired orbit can be simulated. An advantage of utilizing this model in conjunction with 6 DOF dynamics is that

the satellite is not constrained to a single or set of predetermined orbits but instead orbital transfers and maneuvers can be modeled together with the attitude.

2. Atmospheric Model

At LEO, the atmospheric density and composition have a direct impact on the satellite's attitude especially when one considers its low mass and the size of the solar panels relative to the body. Using the MSISE90 atmospheric model it is possible to estimate the density, temperature, and composition of the atmosphere as well as the number densities of its components at a specified altitude on the ECEF.[5] Data from the NRLMSIS-00 (an updated version of MSISE90) is also used since it contains additional data on Oxygen particles at altitudes above 500 km.[6]

3. World Magnetic Model

The last component of the environmental model is a representation of the Earth's magnetic field given by the 2010-2015 World Magnetic Model (WMM). This model provides magnetic intensity, inclination, and declination information and a complete geometry of the field in a -1 km to 850 km range in the NED frame.[7]

C. External Disturbance Models

For a typical satellite in LEO, there are four significant attitude disturbances: aerodynamic drag, magnetic field toques, gravity-gradient torques, and impingement by solar radiation.[8] These are regarded as separate pure moments which correspond to the disturbance term in Eq. (2).

1. Aerodynamic Drag

The aerodynamic torques are produced by the atmospheric particles colliding with the satellite surface. Collisions occur at a higher frequency during maximum solar activity resulting in larger disturbances. This worst case scenario has been assumed for all aerodynamic calculations. The aerodynamic torques on the satellite are estimated by Eq. (10)

$$\boldsymbol{T_{aero}} = \frac{1}{2}\rho \boldsymbol{V_\infty^2} C_m S l \tag{10}$$

At a nominal altitude of 500 km the NRLMSISE00 model gives an atmospheric composition of 94% O and 6% N. The number and mass densities are $n = 3.769 \times 10^{14}$ $\mathrm{kg/m^{-3}}$ and $\rho = 1.02 \times 10^{11}$ $\mathrm{kg/m^{-3}}$ respectively and the temperature is 1491K. The mean free path between particles $\lambda = 27.33$ km which compared with a reference length l of 0.1 m results in a Knudsen number, $Kn = \lambda/l = 273,300$, indicating that the satellite lies in the free molecular flow regime.

Given the previous statement, the moment coefficients of the satellite were calculated using the direct solution Monte Carlo (DSMC) program DAC97, which employs algorithms based on the methods described by G.Bird.[9] A variable hard sphere model (VHS) has been assumed for the collisions between the particles (O and N) and the satellite. V has been assumed to be 7.612 $\mathrm{km/s}$, which is equivalent to the mean orbital speed at a 500 km circular orbit.

A total of 1369 runs of the DAC97 code have been performed on the ARAPAIMA body geometry for 37 different α and β values. The angle of attack was varied between -90° and 90° in steps of 5°; the sideslip angle was similarly varied between 0° and 180° (the angle of attack and the sideslip angle are defined as seen in figure 4). The DSMC results are used to form 2D look-up tables which map the drag and moment coefficients as functions of α and β as shown in figure 5. Together with the total mass density obtained from the MSISE90 model we can use Eq. (10) to calculate the aerodynamic disturbance torques at any orientation (figure 6, subfigure (a)). The maximum force coefficient corresponding to the drag coefficient in general aerodynamic terms is approximately 2.0 which is within the expected range (2.0-2.2) for small satellites in LEO.[8]

2. Magnetic Residual Moment

The magnetic disturbance torque has two major sources: the force produced on a point charge by the magnetic component of the Lorentz force, and the torque experienced by an aspheric paramagnetic body

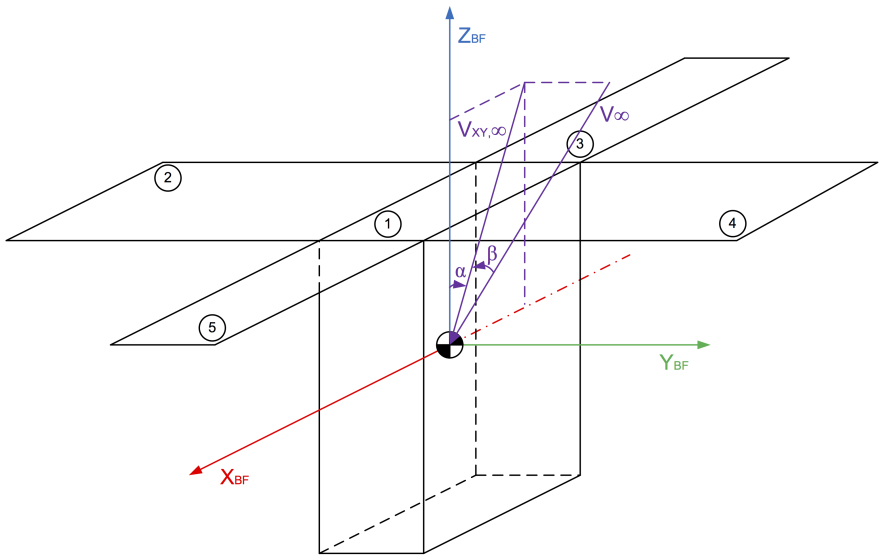

Figure 4: Angle of attack (α) and sideslip angle (β) definitions.

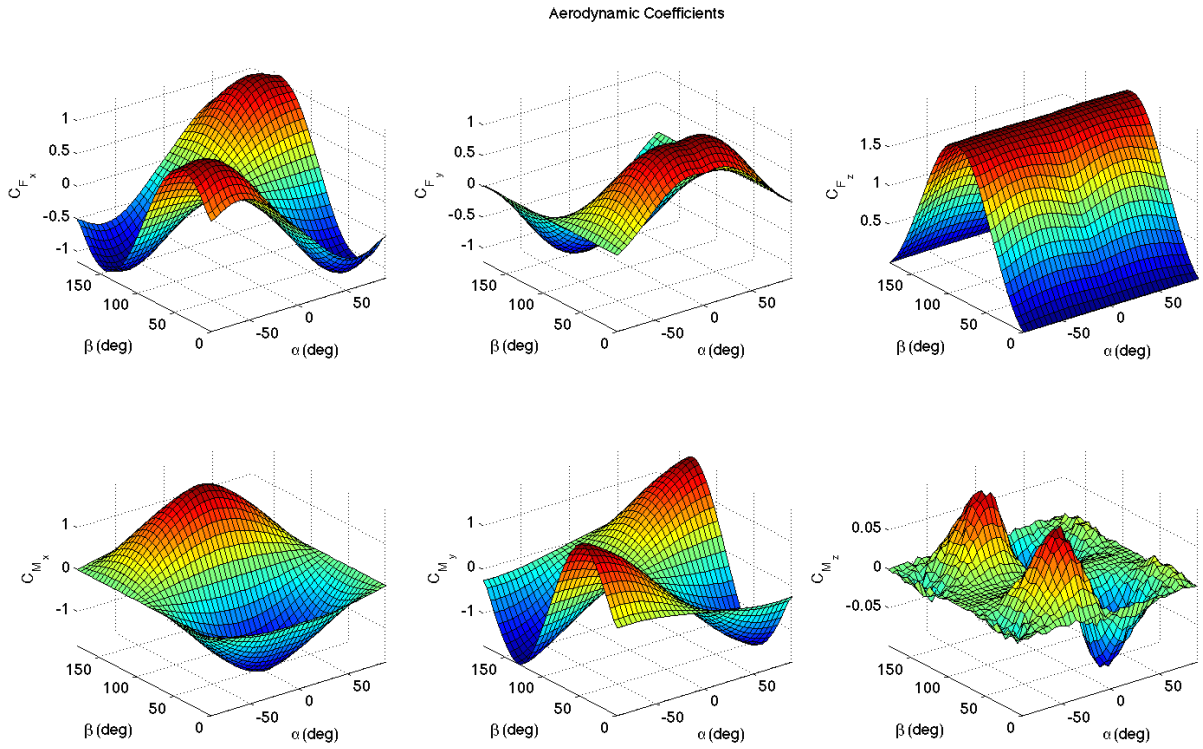

Figure 5: Force and moment coefficient of the ARAPAIMA satellite as functions of its orientation in terms of α and β.

which, in the absence of other torques, aligns its long axis with the local magnetic field. This means that all electrically conducting parts of the satellite contribute charges and produce time varying magnetic fields. Due to the complex nature of evaluating these disturbance torques, we resort to empirical data in order to estimate their effect. An estimate of the maximum magnetic torque can be obtained by combining all contributing magnetic effects into a residual dipole moment specific to the satellite body and exposing it to the environmental magnetic field.[8,10]

$$\boldsymbol{T_{rmm}} = \boldsymbol{m_{rmm}} \times \boldsymbol{B_E} \tag{11}$$

For the ARAPAIMA satellite, $\boldsymbol{m_{rmm}}$ was approximated to be 0.1 Am^2 aligned with the body y-axis thus $\boldsymbol{m_{rmm}} = [0, 0.1, 0]$ Am^2. Together with the WMM $\boldsymbol{M_{rmm}}$ can be calculated as shown in figure 6, subfigure (b).

3. Gravity Gradient Torque

When a satellite's center of mass does not coincide with its center of gravity, the variation of the Earth's gravitational field over the volume of the spacecraft produces torques which in the absence of other disturbances will try to align one of the body's principal axes with the local gravity field vector.[11] This disturbance is easily calculated by

$$\boldsymbol{M_{gg}} = \frac{3\mu}{|\boldsymbol{r}|^3}(\hat{\boldsymbol{r}}) \times \boldsymbol{J}\hat{\boldsymbol{r}} \tag{12}$$

The gravity gradient disturbance contribution to the attitude dynamics can be calculated by evaluating Eq. (12) along the satellite's trajectory. The resulting moments are shown in figure 6, subfigure (c).

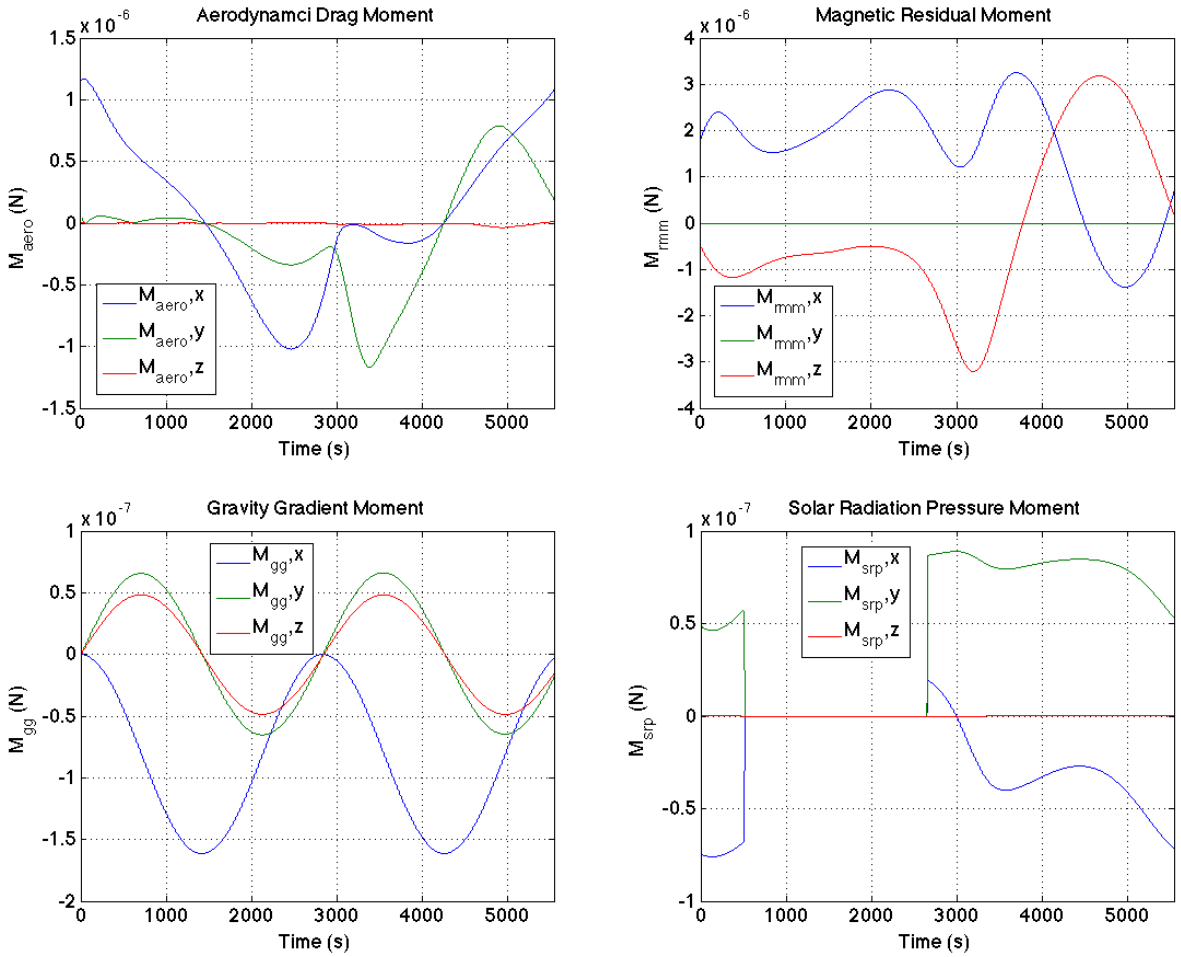

Figure 6: External disturbance torques acting on satellite body for a 1 orbit period

4. *Solar Radiation Pressure*

When solar photons collide with a satellite, the momentum exchange between sunlight and the body surface results in a net pressure force called solar radiation pressure. This pressure is a complex function of the shape and optical properties of the satellite as well as the shading and solar intensity Φ. The worst case scenario is given by Eq. (13) where Φ is taken from an STK simulation for the day of January 1st, 2015.

$$\boldsymbol{M_{srp}} = \frac{\boldsymbol{\Phi} f_s S_s (1+\xi) l_s}{c} \tag{13}$$

The resulting moment is shown in figure 6, subfigure (d).

D. Internal Disturbance Models

External factors are not the only sources of disturbances for a satellite; moving parts and other mechanical interfaces also produce undesirable torques. Many of these internal disturbances are also produced or exacerbated as a result of active control. Because there is no ideal way to mitigate them, the controller must be able must be able to minimize both external and internal torques.

1. *Solar Panel Flexible Modes*

In order to deploy properly, the solar panel hinges are loaded with springs which rotate upon release. In order for the rigid body dynamics outlined in section A to be valid the flexible joints must be modeled such that any moment or force resulting from their movement can be folded into the pre-existing dynamic equations. If we regard the solar panels as rigid bodies the joints can be modeled as a torsion spring by

$$\boldsymbol{M_p} = \boldsymbol{J_p}\ddot{\boldsymbol{\theta}}_{\boldsymbol{p}} + b\dot{\boldsymbol{\theta}}_{\boldsymbol{p}} + k\boldsymbol{\theta_p} \tag{14}$$

The resulting moment $\boldsymbol{M_p}$ can now simply be added to Eq. (2) as a disturbance. Although small in comparison to the external disturbances (figure 7), modeling this reaction is important in order to monitor and avoid exciting structural modes through control actuation.

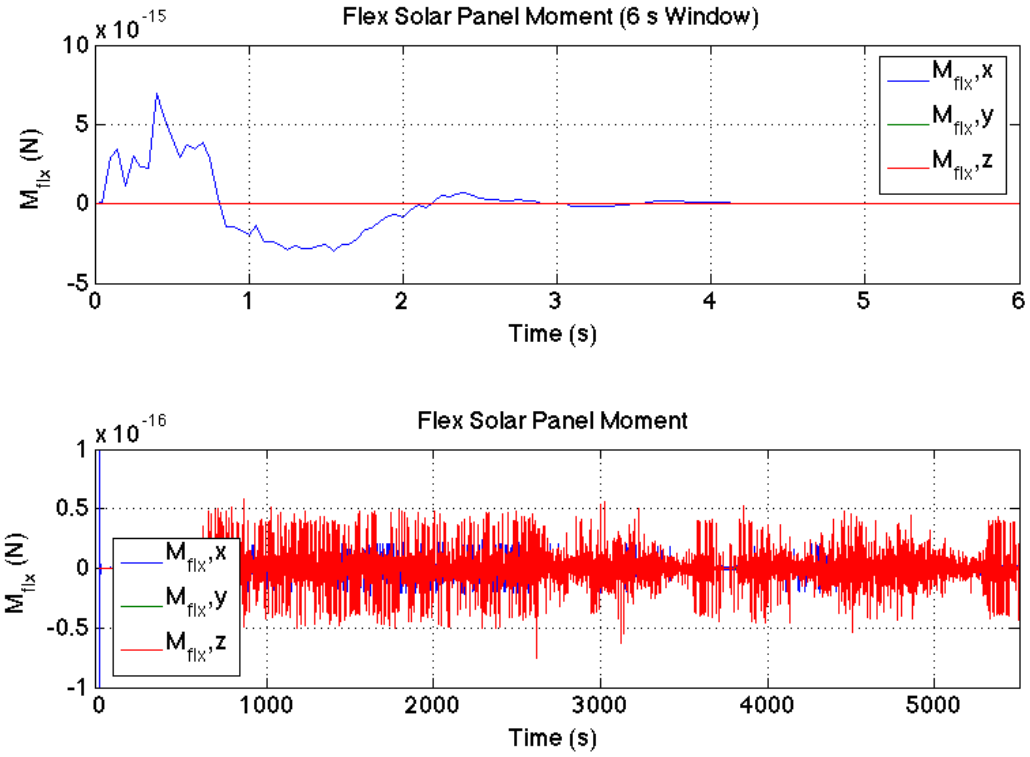

Figure 7: Flexible solar panel disturbance moment.

2. *Propellant Slosh*

Even in microgravity, liquid propellant slosh contributes directly to attitude destabilization. In the case of the ARAPAIMA mission, slosh can hinder mission completion by introducing unwanted angular momentum which could result in a deviation from trajectory during orbital maneuvers or in oscillations of the pointing axis which prevent sufficiently stable imaging. For this reason, a simple yet fairly accurate spring-mass-damper equivalent mechanical model was incorporated in the simulation. This model takes into account the propellant's behavior through the Weber, Froude and Bond numbers and results in the following moment equation proposed by Dodge[12] in terms of angular (θ_{sl}) and linear (x_{sl}) displacements

$$M_{sl} = -(J_{x,0} + m_{sl,0}h_0^2)\theta_{sl} - \Sigma m_{sl,n}h_{sl,n}(\ddot{x}_{sl,n} + H_{sl,n}\theta_{sl,0}) + g\Sigma m_{sl,n}x_{sl,n}. \tag{15}$$

Note that, due to the nature of the mass-spring-damper representation Eq. (15), needs to be modified according to the expected motion along each axis (especially depending on the alignment of the thrusters). The x-axis implementation is given above. The output on all three axes for one orbit can be seen in figure 8.

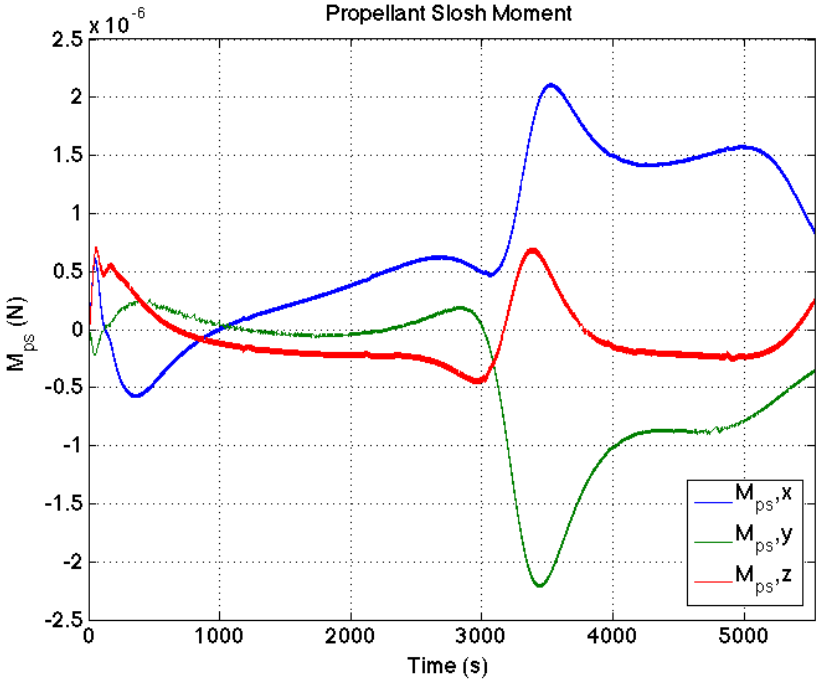

Figure 8: Propellant slosh disturbance moment.

E. Actuator Model

Originally the ARAPAIMA mission relied on reaction wheels to perform attitude control, however, these were still dependent on the RCS thrusters in order to periodically despin the flywheels. This dependency coupled with volume, mass, and power constraints led to the decision of eliminating the reaction wheels in favor of an RCS thruster actuated control system. A trade study focusing on propellant consumption and attitude performance was made to ensure the change would not affect the satellite's ability to complete the mission.

1. *Reaction Wheels*

The reaction wheels (RWs) were modeled as brushed DC motors with an open-loop transfer function given by

$$\frac{\omega_{rw}}{V} = \frac{K_m}{(R_m J_{rw})s + K_m^2} = \frac{K}{\tau s + 1} \tag{16}$$

Adding a simple PI controller yields the following closed loop transfer function.

$$\frac{\Omega_{rw}}{V} = \frac{Kk_{i,rw}}{\tau s + (Kk_{p,rw} + 1)s + Kk_{i,rw}} \tag{17}$$

Acknowledging that the reaction wheel angular momentum can be calculated as

$$\boldsymbol{H_{rw}} = \boldsymbol{J_{rw}}\boldsymbol{\omega_{rw}}$$

then the torque applied to the satellite is given as a function of its angular velocity

$$\boldsymbol{M_{rw}} = \boldsymbol{\Omega} \times \boldsymbol{H_{rw}} \tag{18}$$

The propellant usage needed to offload the reaction wheels is determined by calculating the required thruster burn time and the saturation time of each reaction wheel. The burn time is dependent on the mass flow rate $\dot{m_{prop}}$ and specific impulse I_{sp} of the propellant. The saturation time is dependent on the reaction wheel nominal angular momentum and the root square sum of the disturbance torques acting on the satellite body.

$$t_{burn} = \frac{h}{2Tl_{rcs}} \tag{19}$$

$$\dot{m}_{prop} = \frac{T}{I_{sp}g_e} \tag{20}$$

Thus the amount of propellant used per offload maneuver is calculated by:

$$m_{b,rw} = \dot{m}_{prop}t_{burn} \tag{21}$$

For a disturbance scenario corresponding to that shown in figure 6, evaluating Eq. (21) over time estimates a total of 0.945 kg of propellant per orbit needed to offload the reaction wheels. Note that this is a worse case scenario which assumes constant imaging mode pointing requirements (1 arcmin).

2. RCS Thrusters

Using pulse width modulation techniques the thrusters can be "throttled" at 1% increments of the maximum thrust value over a linear region made possible by rapid solenoid valve actuation. When operated within a range of 0-60 Hz, the mass flow rate remains linear through the entire duty interval (figure 9). When operated at higher frequencies the linear region begins to deteriorate; the current model assumes a $f_{rcs} = 10$ Hz operating frequency.

Building on these properties the RCS thruster model assumes a quantized linear relationship between the commanded and produced thrust where each step size corresponds to a 1% of the maximum thrust value. A graphical representation of this assumption is shown in figure 10.

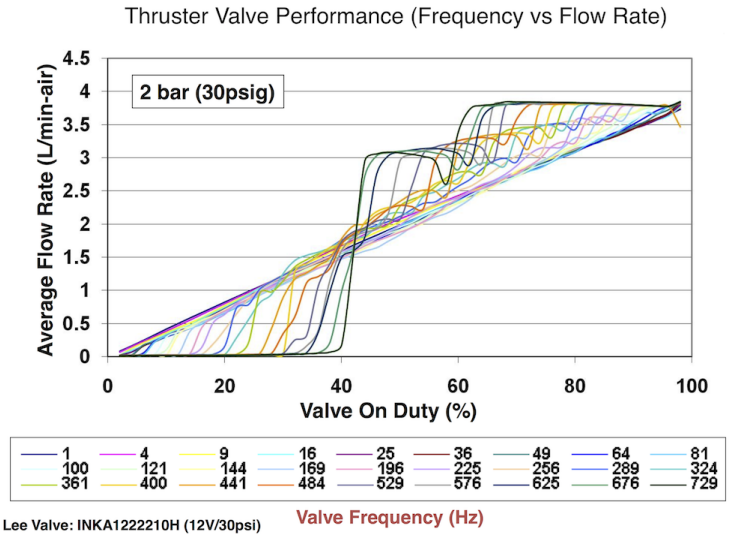

Figure 9: RCS valves mass flow rate performance at different operation frequencies.

This quantized model also introduces a delay which corresponds to the difference in sampling time of the controller, valves, and onboard computer. Because the current simulation assumes the valves operate at a slower frequency than the controller, this delay is

currently equivalent to $\frac{1}{f_{rcs}}$. Equation (22) describes the relationship between the commanded and delayed actuated moment.

$$\begin{aligned} \boldsymbol{M_{cmd,(t)}} &= 2l_{rcs}\boldsymbol{T_{cmd,(t)}} \\ \boldsymbol{M_{act,(t+1)}} &= 2l_{rcs}\boldsymbol{T_{act,(t+1)}} \quad = 2l_{rcs}\boldsymbol{T_{cmd,(t)}} \end{aligned} \tag{22}$$

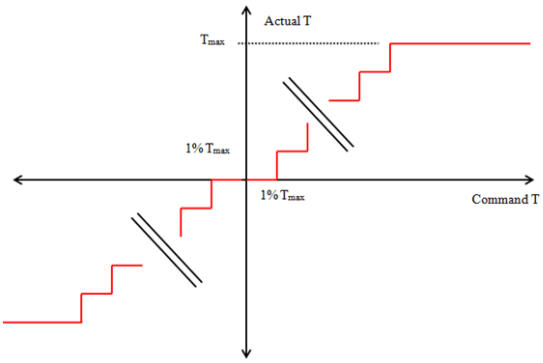

Figure 10: Quantization and saturation of thrust command values.

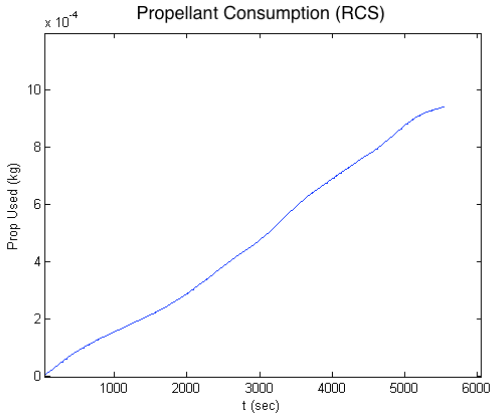

Figure 11: Propellant usage for RCS thruster disturbance rejection.

As a means of direct performance comparison with the reaction wheel actuated control, the same disturbance scenario was presented to the thruster actuated system. The total propellant per orbit needed to reject all exterior disturbances was approximately 0.95 kg as shown in figure 11. Figure 12 compares the pointing performance of both actuators. Given that the pointing performance of both actuators is comparable and the propellant usage is the same for this combination of thrust and propellant specifications, the RWs were removed from the design in order to save mass and volume needed for other components.

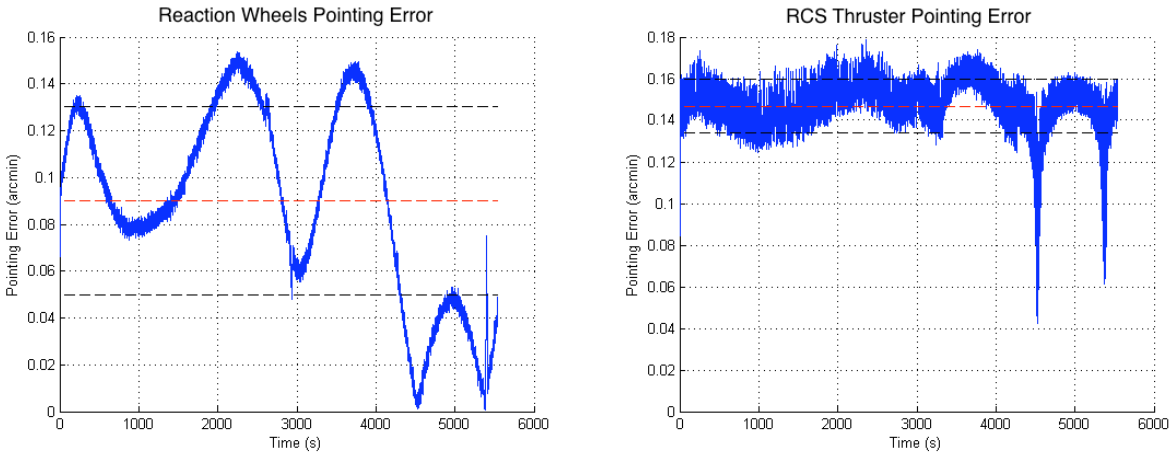

Figure 12: RW and RCS thruster point performance

III. Controller Design

The ARAPAIMA mission requires that its ADCS be able to handle long angle transition maneuvers as well as precise attitude tracking imaging maneuvers. The approach presented here uses a combination of nonlinear eigenaxis control and PID controllers about each axis. For the moment, a periodic switching scheme is presented together with a bump conditioning algorithm with scheduled gains which attempts to smooth the transition between controllers.

A. Eigenaxis Control

The large angle maneuver control law is based on the quaternion feedback regulator proposed by Wie[13] and applied by Pong[14] to CubeSat missions. The controller consists of a linear error quaternion feedback and both linear and nonlinear angular rate feedback which counteract gyroscopic coupling torques.[13] This approach is based on eigenaxis rotations and is analogous to the well known PD controller. It was designed with large angle maneuvers in mind and its global stability as well as its robustness to inertia matrix uncertainty has been proven in relation to various spacecraft applications.[13,15,16] The torque command given by the control law is expressed in the Laplace domain as

$$\boldsymbol{M_{cmd}} = -\boldsymbol{\omega} \times \boldsymbol{J\omega} - \boldsymbol{K_d\omega} - \boldsymbol{K_p\bar{q}_e} \tag{23}$$

where the proportional and derivative gain matrices are given by $\boldsymbol{K_p} = p\boldsymbol{J}$ and $\boldsymbol{K_d} = d\boldsymbol{J}$ respectively; p and d are scalar tuning parameters.

B. PID Control

As with all PD controllers, the lack of an integral term introduces non-zero steady state errors. In order to achieve the high accuracy needed for imaging modes, a simple PID controller is applied about each axis. Taking the vector part of the error quaternion

$$\boldsymbol{M_{cmd}} = -[\boldsymbol{K_p} + \frac{\boldsymbol{K_i}}{s} + \boldsymbol{K_d}s]\boldsymbol{q_{e_v}} \tag{24}$$

where the gains again are the product of the body moment of inertia matrix and scalar tuning parameters.

However, high precision integral controllers are ill suited for large angle maneuvers and are heavily dependent on the magnitude of the error or initial conditions to ensure stability. Therefore, the PID control law is implemented as an extension of the eigenaxis controller which comes into effect once a certain set of circumstances are met. These circumstances are a weighed combination of the current attitude error, its behavior over time, and the current mission operational mode. This way, the eigenaxis controller operates throughout the majority of the maneuvers and ensures the appropriate conditions are met for the PID controller to take over. If the error grows past a predetermined set of bounds, operation will switch back to the eigenaxis controller to prevent instability.

1. Bump Conditioning

The smoothness with which the switch or transfer between controllers occurs is addressed by considering bump conditioning techniques as presented by Peng.[17] Although complex system dynamics prevent completely bumpless transitions, some improvement is achieved by altering Eq. (24) to the following form:

$$\boldsymbol{M_{cmd,(t+1)}} = -\boldsymbol{K_p q_{e_v,(t)}} - \frac{\boldsymbol{K_i}}{s}(K_t(\boldsymbol{M'_{cmd,(t)}} + \boldsymbol{M_{cmd,(t)}}) + \boldsymbol{q_{e_v,(t)}}) - \boldsymbol{K_d} s\boldsymbol{q_{e_v,(t)}} \tag{25}$$

Note that the difference between Eq. (24) and Eq. (25) lies on how the integral action is addressed. Because the eigenaxis controller lacks integral terms, this kind of conditioning in only useful when switching to PID control; similar corrections are unnecessary when operation switches back to eigenaxis control.

The effectiveness of Eq. (25) can be augmented by the use of scheduled gains. Building on the notion that integral controllers are sensitive to abrupt changes, linear transitions can be scheduled such that the gain values are identical to those of the eigenaxis controller at the instant when the switch to PID occurs.

This further smooths the introduction of integral action into the system since $\boldsymbol{K_i}$ would start at zero and then increase according to some liner function of time $f(t)$ as:

$$\begin{aligned} p_2 &= p_1 + f(t)(p_2 - p_1) \\ i_2 &= i_1 + f(t)(i_2 - i_1) \\ d_2 &= d_1 + f(t)(d_2 - d_1) \end{aligned} \tag{26}$$

where $f(t)$ ranges from 0 to 1. The slope of $f(t)$ then controls the abruptness of the transition.

IV. Numerical Simulation and Results

A numerical simulation model has been prepared in a combined MATLAB and Simulink environment. This setup has the advantage of including many blocksets and functions which simplify the calculations needed, particularly the built-in interface for the environmental models mentioned in section B. The model runtime was set to simulate a single 92 min orbit in close proximity (250 m) to the RSO using a 4th order fixed-step extrapolation integrator (ode14x) with a step size of 0.05 s. The RSO and satellite orbits were determined from STK simulations used to design the ARAPAIMA mission trajectories. These give us the required $\boldsymbol{\omega_{cmd}}$ and $\bar{\boldsymbol{q}}_{\boldsymbol{cmd}}$ commands needed to track the RSO (i.e. controller commands).

The model takes into account all dynamics outlined in section II and applies both control laws discussed in section III. However, due to the short span of the simulation, the switching between controllers has been made periodic in order to show the characteristics of both control laws. Figure 13 shows the combined internal and external disturbance torques acting on the body throughout the simulation. For the purposes of initializing all environmental models, the date is assumed to be January 1st 2015. This date also corresponds to the date of the RSO orbit simulation.

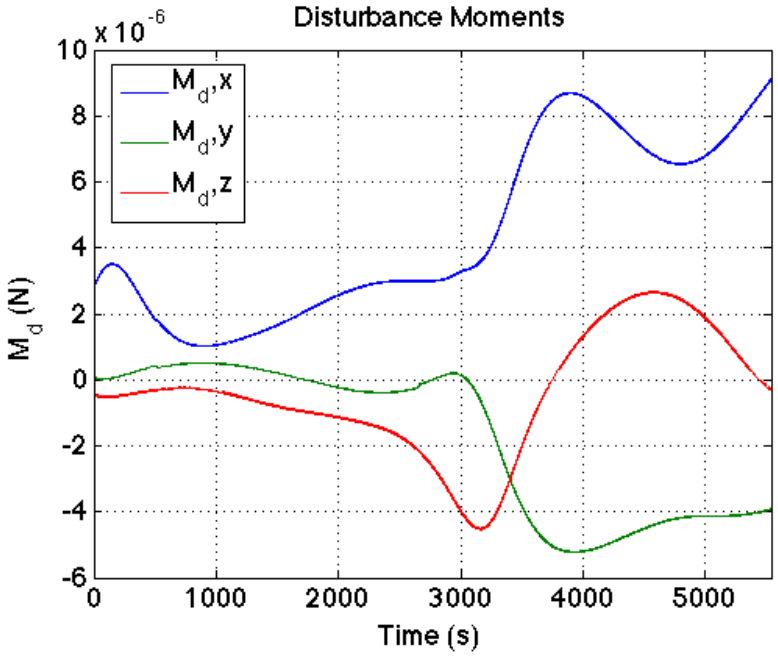

Figure 13: Flexible solar panel disturbance moment.

The eigenaxis controller was tuned so that the scalar tuning parameters $p_1 = 8$, $d_1 = 0$, and $i_1 = 0$ whereas the PID controller was tuned so that $p_2 = 2$, $d_2 = 15$, and $i_2 = 0.1$.Figure 14 shows the overall pointing performance of the satellite for different control settings. In order to assess the advantages of switching while still quantifying the smoothness of the transition between controllers three different scenarios are examined. The first (figure 14, subfigure (a)) shows the pointing performance with no bump conditioning or gain scheduling. This gives a steady state error of 0.18 arcmin for the eigenaxis controller and 0.025 for the PID controller. However, the switch causes significant overshoot (1-7 arcmin). Note that the PID is

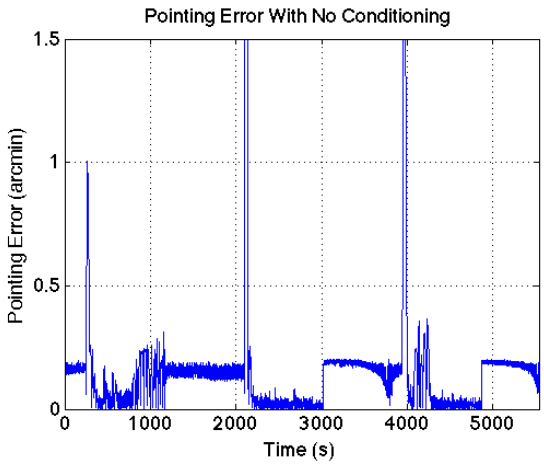

(a) Pointing performance with no bump conditioning and no gain scheduling

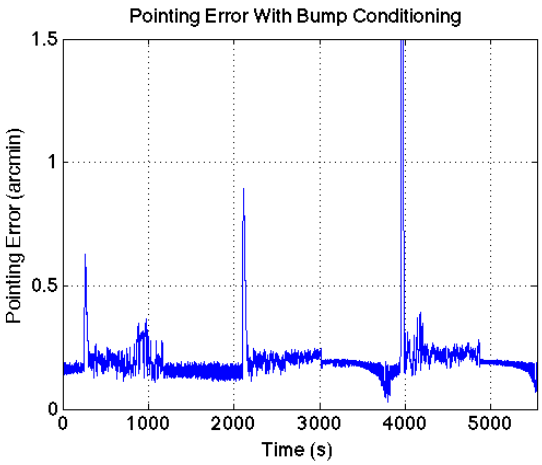

(b) Pointing performance with bump conditioning but no gain scheduling

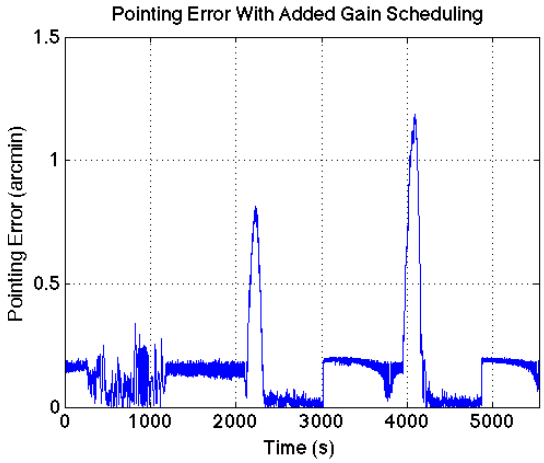

(c) Pointing performance with bump conditioning and gain scheduling

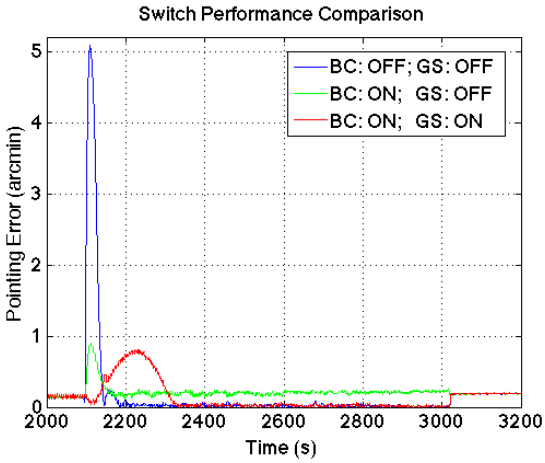

(d) Bump conditioning performance comparison

Figure 14: Switching controller performance.

sensitive to changes in angular acceleration whereas the eigenaxis controller remains at steady state except for short jumps where the accuracy improves.

The second scenario (subfigure (b)) shows the performance when the PID controller is as in Eq. (25). This offers noticeable improvement in the switch overshoot (0.65-3 arcmin) but because the K_t term remains non-zero after the transient period, it offers no improvement on the overall performance. This is fixed in the third scenario when gain scheduling is introduced. The scheduled gains assume a transient period of 200 s during which the $\boldsymbol{K_p}$, $\boldsymbol{K_i}$, $\boldsymbol{K_d}$ gains are changed according to Eq. (26) and are shown in figure 15. The bump conditioning gain does not behave this way, but instead is a fixed non-zero value during the transient period and is zero elsewhere. This approach further improves the overshoot (0.70-1.20 arcmin) and restores the improvement on pointing performance seen in the first scenario yet at the cost of longer transition periods. Subfigure (d) gives a side by side comparison of the bump conditioning given by each approach.

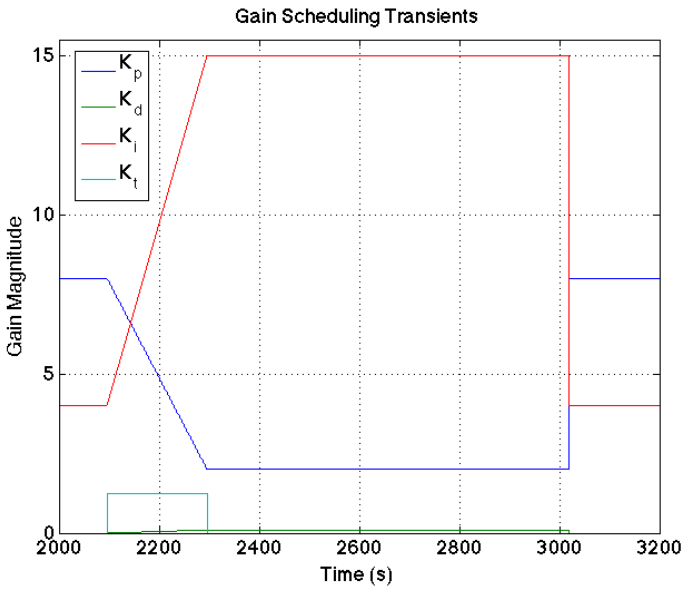

Figure 15: Gain scheduling transients corresponding to those in figure 14, subfigure (d)

A. Future Work

While the current results are promising, there remain ways in which the fidelity of the model might be improved in order to further test and prove the stability of the ADCS. As the control laws must be implemented on the satellite on-board computer, the entire model must be discretized and made to account for the different sampling rates and inherent delays of digital implementation. In direct relation is the matter of hardware noise and interference along with a corresponding filter design to compensate for the rate transition and inaccuracies of sensor readings. Figure 16 gives an example of controller performance with unfiltered sensor noise; the noise levels are based on the real mission hardware.

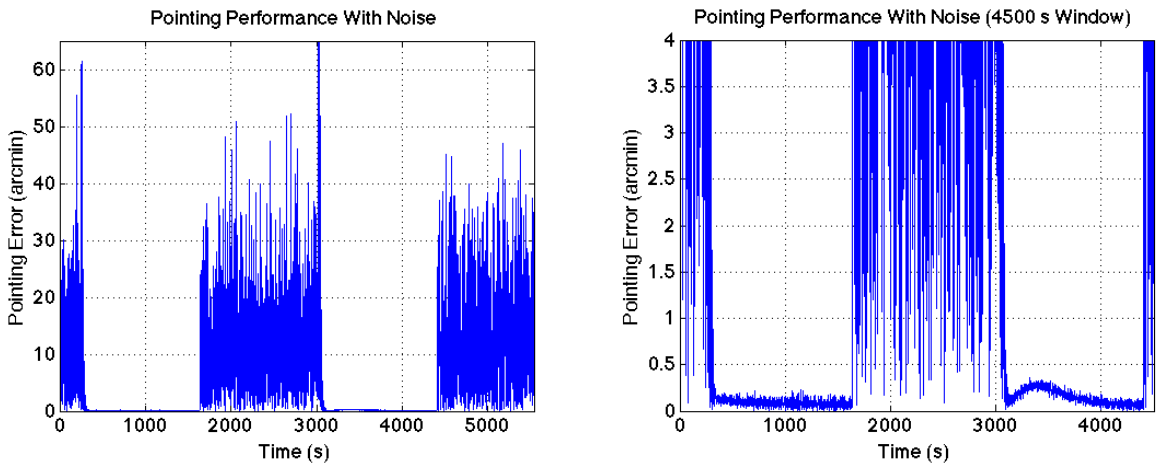

Figure 16: Pointing error with sensor noise in the system.

It is clearly shown how the sensor noise has a significant impact on pointing accuracy especially while during eigenaxis control since from Eq. (23) we can see that it is directly susceptible to both STR and IMU noise. The PID maintains an accuracy of 0.5 arcmin but in a real scenario an IMU samples at a much faster rate than a STR so attitude estimate propagation would still be affected by IMU noise, decreasing the PID performance.

V. Conclusion

The purpose of this paper has been to demonstrate the validity of the ADCS design approach as well as the capability of CubeSat class satellites to contribute to current areas of interest using COTS products and without the necessity of a multi-million dollar budget. Going further than a feasibility analysis the aim is to prove through testing and design the performance of a real system that is able to extend into hardware integration and implementation. Through the use of proven models and methods and a combination thereof it has been shown that the hardware (through specifications) and design are able to achieve the performance stipulated in the mission criteria. Future work and necessary improvements are expected to increase the quality and reliability of the working system.

Acknowledgments

Special thanks to Luis A. Sánchez for his work in developing the numerical simulation and reviewing the material included in this paper.

Special thanks are also in order to the members of the ARAPAIMA mission, especially those of the ADCS subsystem which have given up many free hours in order to help achieve this work.

Additional thanks go to the supporting professors at Embry-Riddle Aeronautical University for their guidance, dedication, and support.

References

[1]Shuster, M. D., "A Survey of Attitude Representations," *The Journal of the Astronautical Sciences*, Vol. 41, No. 4, October-December 1993, pp. 439–517.

[2]Simulink, M. ., *Aerospace Blockset User's Guide 2013a*, The MathWorks Inc., Natick, Massachusetts, 3rd ed., March 2013.

[3]Schutz, B., Tapley, B., and Born, G. H., *Statistical Orbit Determination*, Elsiever Academic Press, 2004.

[4]MATLAB, *Aerospace Toolbox User's Guide 2013a*, The MathWorks Inc., Natick, Massachusetts, 2nd ed., March 2013.

[5]Hedin, A. E., "MSIS-E-90 Atmoshpere Model," .

[6]Picone, M., Hedin, A., and Drob, D., "NRLMSISE-00," .

[7]Maus, S., Macmillan, S., McLean, S., Hamilton, B., Thomson, A., Nair, M., and Rollins, C., "The US/UK World Magnetic Model for 2010-2015," Tech. rep., NOAA NESDIS/NGDC, 2010.

[8]Wertz, J. R., Everett, D. F., and Puschell, J. J., *Space Mission Engineering: The New SMAD*, Microcosm Press, 4th ed., 2011.

[9]Bird, G. A., *Molecular Gas Dynamics And The Direct Simulation Of Gas Flows*, Oxford University Press, USA, 1994.

[10]Inamori, T., Sako, N., and Nakasuka, S., "Compensation of time-variable magnetic moments for a precise attitude control in nano-and micro-satellite missions," *Advances in Space Research*, Vol. 48, No. 3, 2011, pp. 432–440.

[11]Curtis, H., *Orbital Mechanics for Engineering Students*, Elsiever Aerospace Engineering Series, Butterworth-Heinemann, 3rd ed., 2013.

[12]Dodge, F. T., *The New Dynamic Behavior of Liquids in Moving Containers*, Southwest Research Institute, 2010.

[13]Wie, B., Weiss, H., and Arapostathis, A., "Quaternion Feedback Regulator for Spacecraft Eigenaxis Rotations," *Journal of Guidance, Control, and Dynamics*, Vol. 12, No. 3, May-June 1989, pp. 375–380.

[14]Pong, C. M., Lim, S., Smith, M. W., Miller, D. W., Villaseñor, J. S., and Seager, S., "Achieving high-precision pointing on ExoplanetSat: Initial Feasibility Analysis," *MIT Open Access Articles*, 2010.

[15]Wie, B., "Quaternion Feedback For Spacecraft Large Angle Maneuvers," *Journal of Guidance, Control, and Dynamics*, Vol. 8, No. 3, 1985, pp. 360–365.

[16]Wie, B. and Lu, J., "Feedback Control Logic for Spacecraft Eigenaxis Rotations Under Slew Rate and Control Constraints," *Journal of Guidance, Control, and Dynamics*, Vol. 18, No. 6, 1995, pp. 1372–1379.

[17]Peng, Y., Vrancic, D., and Hanus, R., "Anti-Windup, Bumpless, and Conditioned Transfer Techniques for PID Controllers," *Control Systems, IEEE*, Vol. 16, No. 4, 1996, pp. 48–57.